Vaz-Romero, A.; Rodríguez-Martínez, J.A (2016). On the interplay between material flaws and dynamic necking. *Mechanics Research Communications,* vol. 72, pp. 53-58.

DOI: https://doi.org/10.1016/j.mechrescom.2016.01.003

On the interplay between material flaws and dynamic necking

A. Vaz-Romero*, J. A. Rodríguez-Martínez

Department of Continuum Mechanics and Structural Analysis. University Carlos III of Madrid. Avda. de la Universidad, 30. 28911 Leganés, Madrid, Spain

Abstract

In this paper we investigate the interplay between material defects and flow localization in elastoplastic bars subjected to dynamic tension. For that task, we have developed a 1D finite difference scheme within a large deformation framework in which the material is modelled using rate-dependent J_2 plasticity. A perturbation of the initial yield stress is introduced in each node of the finite difference mesh to model localized material flaws. Numerical computations are carried out within a wide spectrum of strain rates ranging from 500 s^{-1} to 2500 s^{-1}. On the one hand, our calculations reveal the effect of the material defects in the necking process. On the other hand, our results show that the necking inception, instead of being a random type process, is the deterministic result of the interplay between the mechanical behaviour of the material and the boundary conditions. This conclusion agrees with the experimental evidence reported by Rittel et al. [1] and Rotbaum et al. [2].

Keywords:
Dynamic stretching, Numerical simulations, Material defects, Flow localization

1. Introduction

Whether dynamic necking in elastoplastic solids is a random or deterministic process remains as an open question. This issue, which has triggered critical debates in the Solid Mechanics community during the last decade, has been typically addressed using two different uniaxial tensile configurations [3].

On the one hand, we have the radial expansion of ductile rings [4, 5, 6]. The geometric and loading symmetries of this problem nearly eliminate the effects of wave propagation before the onset of necking, which reveals the *true* mechanical properties of the material. For years, it was accepted that the multiple localization pattern which precedes fragmentation in the ring expansion test is a random process, controlled to a large extent by geometric and material defects. However, some recent publications [7, 8] have raised the possibility that the localization process becomes deterministic for sufficiently high expansion velocities. The increase of the inertia forces with the loading rate helps to regularize the problem and promotes the emergence of uniform necking patterns which reveal the deterministic nature of the localization process.

On the other hand, we have the impact testing of *linear* tensile specimens [9, 10]. The sample, initially at rest, is subjected to a sudden axial velocity which, unlike what happens in the ring expansion test, leads to the generation of stress waves. It has been frequently assumed in the literature that, despite the stress waves intervention within the specimen, the necking inception in the impact tensile test is a random process. However, recent experimental works [1, 2] suggested that flow localization in the dynamic tensile test is the deterministic result of the interplay between material behaviour, specimen geometry and boundary conditions. In this paper we develop a numerical methodology which supports such experimental finding. We carry out computations using a finite difference model in which material flaws are included. Our results indicate that wave propagation phenomena control, to a large extent, flow localization in elastoplastic specimens subjected to impact tensile loading.

2. Constitutive equations

The material behaviour is described by a hypoelastic-plastic constitutive model which follows the standard principles of Huber-Mises plasticity.

The evolution equation for the Kirchhoff stress $\boldsymbol{\tau}$ is:

$$\boldsymbol{\tau}^{\nabla} = \mathcal{L} : \mathbf{d}^{\mathrm{e}} \tag{1}$$

where $\boldsymbol{\tau}^{\nabla}$ is the Green-Naghdi objective derivative of the Kirchhoff stress tensor. We have followed the works of Holzapfel [11] and Sumelka [12], and use the Kirchhoff stress in the formulation of the constitutive equations. This is considered the most directly available stress measure when an elastic reference state is considered. More-

*Corresponding author. Tel. +34 916246015; Fax: +34 916249430. E-mail address: avazrome@ing.uc3m.es

over, the fourth order isotropic elasticity tensor $\mathcal{L}$ and the elastic rate of deformation tensor $\mathbf{d}^{\mathrm{e}}$ are defined as follows:

$$\mathcal{L} = 2G\mathcal{I} + \lambda \mathbf{I} \otimes \mathbf{I} \tag{2}$$

$$\mathbf{d}^{e} = \mathbf{d} - \mathbf{d}^{p} \tag{3}$$

where G and λ are the Lamé's constants, $\mathcal{I}$ is the fourth order identity tensor and $\mathbf{I}$ is the second order identity tensor. $\mathbf{d}$ and $\mathbf{d}^{\mathrm{p}}$ are the total and plastic rate of deformation tensors, respectively.

The yield function f is written as:

$$f = \bar{\tau} - \sigma_Y = 0 \tag{4}$$

where the equivalent stress $\bar{\tau}$ and the yield stress σ_Y are defined as follows:

$$\bar{\tau} = \sqrt{\frac{3}{2}\left(\mathbf{s} : \mathbf{s}\right)} \tag{5}$$

$$\sigma_Y = A + B\left(\bar{\varepsilon}^{p}\right)^{h}\left(\frac{\dot{\bar{\varepsilon}}^{p}}{\dot{\varepsilon}_{ref}}\right)^{m}\left(\frac{T}{T_{ref}}\right)^{-\mu} \tag{6}$$

where $\mathbf{s} = \boldsymbol{\tau} - \frac{1}{3}\left(\boldsymbol{\tau} : \mathbf{I}\right)\mathbf{I}$ is the deviatoric part of the Kirchhoff stress tensor, $\dot{\bar{\varepsilon}}^{p} = \sqrt{\frac{2}{3}\left(\mathbf{d}^{\mathrm{p}} : \mathbf{d}^{\mathrm{p}}\right)}$ is the equivalent plastic strain rate, $\bar{\varepsilon}^{p} = \int_0^t \dot{\bar{\varepsilon}}^{p}\left(\xi\right)\mathrm{d}\xi$ is the equivalent plastic strain and T is the current material temperature. A, B, h, m and μ are material parameters while $\dot{\varepsilon}_{ref}$ and T_{ref} are the reference strain rate and temperature.

The flow rule is given by:

$$\mathbf{d}^{\mathrm{p}} = \frac{\partial f}{\partial \boldsymbol{\tau}}\dot{\bar{\varepsilon}}^{p} = \frac{3}{2}\frac{\mathbf{s}}{\bar{\tau}}\dot{\bar{\varepsilon}}^{p} \tag{7}$$

The formulation of the constitutive model is completed by introducing the Kuhn–Tucker loading/unloading complementary conditions:

$$\dot{\bar{\varepsilon}}^{p} \geq 0, \quad f \leq 0, \quad \dot{\bar{\varepsilon}}^{p} f = 0 \tag{8}$$

and the consistency condition during plastic loading:

$$\dot{f} = 0 \tag{9}$$

In the calculations of this paper we use the constitutive parameters corresponding to the AISI 430 steel [13]. These are given in Table 1.

3. Governing equations

We consider a cylindrical bar of initial length $L = 6\ mm$ and cross-section diameter $\Phi = 3\ mm$ subjected to dynamic stretching. Within a 1D analysis we do not need to specify the shape of the cross-section area, nevertheless we consider that the bar is cylindrical (to calculate the force in the sample, see Fig. 2), as a typical tensile specimen. The dimensions of the bar correspond to samples used in Split Hopkinson Tensile Bar experiments [2, 14]. The problem is posed in one-dimensional form.

The relation between the Eulerian z and the Lagrangian coordinate Z ($0 \leq Z \leq L$) is given by:

$$z = Z + U_Z \tag{10}$$

where U_Z is the displacement along the axial direction. The logarithmic strain ε_Z and strain rate $\dot{\varepsilon}_Z$ along the axial direction are given by:

$$\varepsilon_Z = ln\left(1 + \partial U_Z/\partial Z\right) \tag{11}$$

$$\dot{\varepsilon}_Z = \partial \varepsilon_Z/\partial t \tag{12}$$

The fundamental equations, formulated in Lagrangian coordinates, which govern the loading process are given below.

- Mass conservation:

$$\rho_0 = \rho \mathrm{J} \tag{13}$$

  where ρ_0 is the initial material density, ρ is the current density and $\mathrm{J} = e^{(1-2\gamma)\varepsilon_Z}$ is the Jacobian determinant of the deformation gradient tensor, where γ is a material parameter specified in section 4.

- Momentum balance in the axial direction:

$$\rho_0 \Lambda_0 \frac{\partial^2 U_Z}{\partial t^2} = \frac{\partial}{\partial Z}\left(\frac{\Lambda}{\mathrm{J}}\tau_Z\right) \tag{14}$$

  where Λ_0 and Λ are the initial and current cross-section areas of the bar and τ_Z is the Kirchhoff stress along the axial direction.

- Conservation of energy:

$$\rho C_p \frac{\partial T}{\partial t} = k\frac{\partial^2 T}{\partial Z^2} + \beta \tau_Z \dot{\varepsilon}_Z^{\mathrm{p}} \tag{15}$$

  where C_p is the specific heat, k is the conductivity, β is the Taylor-Quinney coefficient and $\dot{\varepsilon}_Z^{\mathrm{p}}$ is the plastic strain rate along the axial direction. The thermoelastic effects are neglected. Note that, for the sake of simplicity, the spatial derivative which appears in the conductivity term is taken as a Lagrangian derivative (small strains in the conductivity term).

- Stress rate: the Green-Naghdi objective derivative, due to the one-dimensional nature of the model, is computed as a simple time derivative:

$$\tau_Z^{\nabla} = \dot{\tau}_Z \tag{16}$$

Considering the domain $[0, L]$, Eqs. (13)-(16) are numerically solved under the following initial and boundary conditions formulated in Lagrangian coordinates:

Symbol	Property and units	Value
ρ_o	Initial density (kg/m^3), Eqs. (13) and (14)	7740
C_p	Specific heat (J/kgK), Eqs. (15) and (28)	460
k	Thermal conductivity (W/mK), Eqs. (15) and (28)	26.1
G	Lamé's constant (GPa), Eqs. (2), (25), (26) and (27)	75.2
λ	Lamé's constant (GPa), Eq. (2) and (26)	146
E	Young's modulus (GPa), Eq. (23)	200
ν	Poisson's ratio	0.33
A	Initial yield stress (MPa), Eq. (6)	175.67
B	Work hardening modulus (MPa), Eq. (6)	530.13
h	Work hardening exponent, Eq. (6)	0.167
$\dot{\varepsilon}_{ref}$	Reference strain rate (s^{-1}), Eq. (6)	0.01
m	Strain rate sensitivity exponent, Eq. (6)	0.0118
T_{ref}	Reference temperature (K), Eq. (6)	300
μ	Temperature sensitivity exponent, Eq. (6)	0.51
β	Taylor-Quinney coefficient, Eqs. (15) and (28)	0.9

Table 1: *Physical constants, elastic parameters and parameters related to the yield stress for AISI 430 steel [13].*

$$U_Z(Z,0)=0;\;\; \tau_Z(Z,0)=0;\;\; T(Z,0)=T_0$$

$$U_Z(0,t)=0;\;\; V_Z(L,t)=V^{imp};\;\; \frac{\partial T(0,t)}{\partial Z}=\frac{\partial T(L,t)}{\partial Z}=0$$

where T_0 is the initial temperature taken as 300 K and V^{imp} is the impact velocity.

4. Finite difference model

Following the works of Zhou et al. [6], Regazzoni et al. [15] and Ravi-Chandar and Triantafyllidis [16], we have developed a 1D finite difference model to describe the mechanical behaviour of elastoplastic bars subjected to dynamic tension. This numerical approach was presented and validated with experiments and finite element calculations in our previous work [17]. In the present paper we only show the main features of the model for completeness.

We define a mesh in the $\{Z-t\}$ plane such that $\Pi=\{Z_j=j\Delta Z,\; t^n=n\Delta t\}$, where $j=0,\ldots,M$ and $n=0,\ldots,N$. The integration space and time steps are $\Delta Z=L/M$ and Δt respectively. The following notations of functions in the mesh nodes $g\left(Z_j,t^n\right)=g_j^n$ are used.

The first and second derivatives of the functions g with respect to the Lagrangian coordinate Z are approximated by:

$$\frac{\partial g}{\partial Z}=\frac{g_{j+1}^n-g_{j-1}^n}{2\Delta Z} \tag{17}$$

$$\frac{\partial^2 g}{\partial Z^2}=\frac{g_{j+1}^n-2g_j^n+g_{j-1}^n}{\Delta Z^2} \tag{18}$$

The first and second derivatives of the functions g with respect to the time t are approximated by:

$$\frac{\partial g}{\partial t}=\frac{g_j^{n+1}-g_j^n}{\Delta t} \tag{19}$$

$$\frac{\partial^2 g}{\partial t^2}=\frac{g_j^{n+1}-2g_j^n+g_j^{n-1}}{\Delta t^2} \tag{20}$$

Displacements update

First we solve the kinematics of the problem and update the displacement U_Z as a function of the Lagrangian coordinate Z. For that task, we rearrange Eq. (14) to obtain Eq. (21):

$$\partial^2 U_Z/\partial t^2=\mathrm{c}_0^2\cdot[1+\partial U_Z/\partial Z]^{-2\gamma}\cdot\left[\frac{\rho}{\rho_0}\left[\left[\frac{\partial^2 U_Z/\partial Z^2}{1+\partial U_Z/\partial Z}\right]\left[1-2\gamma\cdot\left[\ln(1+\partial U_Z/\partial Z)-\varepsilon_Z^p\right]\right]-\right.\right.$$
$$\left.\left.-\;\partial\varepsilon_Z^p/\partial Z\right]+\left[\ln(1+\partial U_Z/\partial Z)-\varepsilon_Z^p\right]\frac{1}{\rho_0}\frac{\partial\rho}{\partial Z}\right] \tag{21}$$

where the following relations have been used:

$$\Lambda = \Lambda_0 \left(1 + \frac{\partial U_Z}{\partial Z}\right)^{-2\gamma} \tag{22}$$

$$\tau_Z = \mathrm{E}\left[\ln\left(1 + \partial U_Z/\partial Z\right) - \varepsilon_Z^p\right] \tag{23}$$

where $\mathrm{c}_0 = \sqrt{\dfrac{E}{\rho_0}}$ is the one-dimensional elastic wave speed, E is the Young's modulus, γ is a material parameter and ε_Z^p is the plastic strain along the axial direction. Note that Eq. (23) comes from the combination of Eqs. (1), (2) and (3) expressed in one-dimensional form.

Following the discretization scheme defined by Eqs. (17)–(20), Eq. (21) leads to Eq. (24) which allows to update the axial displacement:

$$\begin{aligned}(U_Z)_j^{n+1} = [\mathrm{c}_0\Delta t]^2 \left[\frac{2\Delta Z + (U_Z)_{j+1}^n - (U_Z)_{j-1}^n}{2\Delta Z}\right]^{-2\gamma} \left[\frac{\rho_j^n}{\rho_0}\left[\left[\frac{2\left((U_Z)_{j+1}^n - 2(U_Z)_j^n + (U_Z)_{j-1}^n\right)}{\Delta Z\left(2\Delta Z + (U_Z)_{j+1}^n - (U_Z)_{j-1}^n\right)}\right]\right]\left[1 - \right.\right. \\ \left. -2\gamma\left[\ln\left(\frac{2\Delta Z + (U_Z)_{j+1}^n - (U_Z)_{j-1}^n}{2\Delta Z}\right) - (\varepsilon_Z^p)_j^n\right]\right] - \left(\frac{(\varepsilon_Z^p)_{j+1}^n - (\varepsilon_Z^p)_{j-1}^n}{2\Delta Z}\right)\Bigg] + \\ + \frac{1}{\rho_0}\left(\frac{\rho_{j+1}^n - \rho_{j-1}^n}{2\Delta Z}\right)\left[\ln\left(\frac{2\Delta Z + (U_Z)_{j+1}^n - (U_Z)_{j-1}^n}{2\Delta Z}\right) - (\varepsilon_Z^p)_j^n\right]\Bigg] + 2(U_Z)_j^n - (U_Z)_j^{n-1}\end{aligned} \tag{24}$$

Application of Eq. (24) requires to determine the value of γ:

- $\gamma = \nu$ (Poisson's ratio): In the previous time step the material showed purely elastic behaviour.
- $\gamma = 1/2$ (Incompressibility condition): In the previous time step the material deformed elasto-plastically. For the sake of simplicity, we ignore the material compressibility due to elastic straining.

Whether $\gamma = \nu$ or $\gamma = 1/2$ is selected for the first time step depends on the impact velocity. If $\rho_0 c_0 V^{imp} < A$, the impact initially induces only elastic strains in the bar and we take $\gamma = \nu$. If $\rho_0 c_0 V^{imp} \geq A$ the applied velocity induces instantaneous plastic strains in the rod and we take $\gamma = 1/2$.

Stress and temperature update

The stress is updated using a one-dimensional form of the integration scheme developed by Zaera and Fernández-Sáez [18]. Taking advantage of the properties of the return mapping algorithm we obtain:

$$(\tau_Z)^{n+1} = (\tau_Z)_{\text{trial}}^{n+1} - 2\mathrm{G}\Delta\bar{\varepsilon}^p \tag{25}$$

where the trial stress is given by the following expression:

$$(\tau_Z)_{\text{trial}}^{n+1} = (\tau_Z)^n + \lambda\left[\Delta\varepsilon_Z + 2\Delta\varepsilon_R\right] + 2G\Delta\varepsilon_Z \tag{26}$$

where $\Delta\varepsilon_Z$ and $\Delta\varepsilon_R$ are the axial and radial strain increments, respectively.

The update of the equivalent stress is derived from Eq. (25) and takes the form:

$$\bar{\tau}^{n+1} = \bar{\tau}_{\text{trial}}^{n+1} - 3\mathrm{G}\Delta\bar{\varepsilon}^p \tag{27}$$

If the increment of the plastic strains is zero, the stress is updated through the trial elastic stress.

The conservation of energy, Eq. (15), is approximated by the following expression which allows to update the temperature of the material as a function of the Lagrangian coordinate:

$$T_j^{n+1} = \frac{k\Delta t}{\rho C_p}\left[\frac{\left(T_{j+1}^n - 2T_j^n + T_{j-1}^n\right)}{(\Delta Z)^2}\right] + \frac{\beta}{\rho C_p}\bar{\tau}^{n+1}\Delta\bar{\varepsilon}^p + T_j^n \tag{28}$$

In order to obtain the updated stress and the temperature, we calculate the equivalent plastic strain increment $\Delta\bar{\varepsilon}^p$ following the procedure described by Vaz-Romero et al. [13].

5. Localized material defects

We model the material defects (indistinctly referred to as flaws or inhomogeneities) introducing, in each node of the spatial grid, a perturbation of the initial yield stress A, see Eq. (6). This procedure, in which inhomogeneities are modelled as localized perturbations imposed to the nodes of the grid, is in line with the methodologies developed by Rodríguez-Martínez et al. [7], Ravi-Chandar and Triantafyllidis [16] and Zhang and Ravi-Chandar [19] to explore the role played by material and geometrical flaws in the fragmentation of rings and cylinders subjected to dynamic expansion.

Firstly, we determine a maximum percentage of variation for the initial yield stress. Secondly, we assign to each node a random value within the interval defined by this percentage. The random values are generated using a normal distribution (*normrnd* function of MATLAB) with mean parameter $\mu \equiv A = 176$ MPa. Note that this value

corresponds to the unaltered yield stress given in Table 1. The standard deviation σ is determined through an iterative process in order to ensure that the maximum and minimum values in the distribution lie within the interval defined by the selected percentage of variation. As stated by Zhang and Ravi-Chandar [19], this type of statistical distribution for the defect material properties adds a realistic feature to the simulations.

Fig. 1 shows the yield stress statistics corresponding to a maximum percentage of variation of ± 8%. Fig. 1(a) shows the initial yield stress along the normalized coordinate $\bar{Z} = Z/L$ of the bar. We observe that the initial yield stress assigned to all the nodes of the bar lie within the limits defined by the imposed maximum percentage of variation. Fig. 1(b) illustrates the normal probability density function. We observe that the initial yield stress of most nodes falls close to the mean value. While localized perturbations are an idealization of the real material inhomogeneities, we hold that this simple methodology is suitable uncover key some features of the interplay between material flaws and flow localization in the dynamic tensile test.

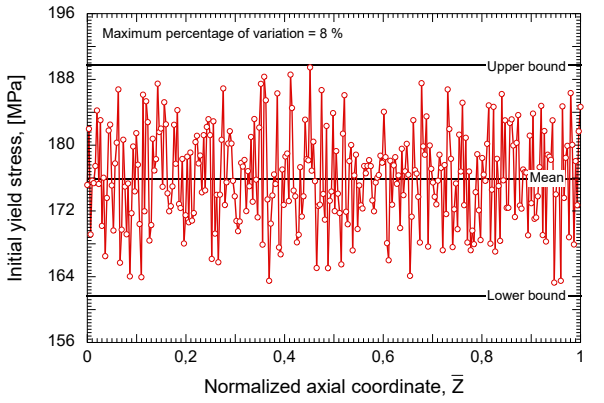

(a)

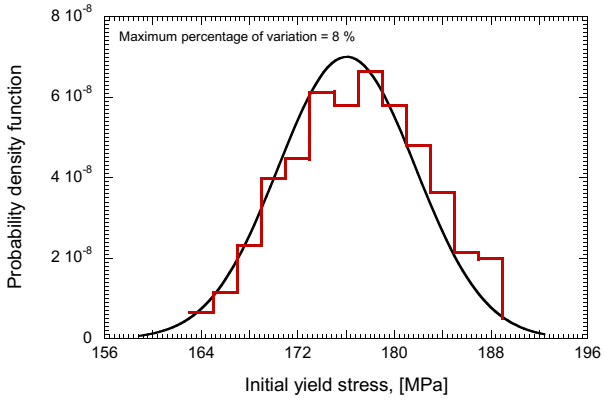

(b)

Figure 1: Yield stress statistics for a maximum percentage variation of ± 8%. The mean and standard deviation of the normal distribution are $\mu \equiv A = 176$ MPa and $\sigma = 6.96$ MPa, respectively. (a) Yield stress versus the normalized coordinate $\bar{Z} = Z/L$. (b) Probability density function along the initial yield stress.

6. Analysis and results

We carry our finite difference calculations within the spectrum of impact velocities $3\ m/s \leq V^{imp} \leq 15\ m/s$ which is attained in typical Split Hopkinson Tensile Bar experiments [1, 2]. The applied velocities lead to initial strain rates which range between 500 s^{-1} and 2500 s^{-1}. We have explored several maximum percentages of variation of the initial yield stress ranging from 0% (intact material) to 12%. The degree of severity of the inhomogeneities increases as the percentage increases, i.e. the percentage of variation of the initial yield stress determines the amplitude of the flaws included in the calculations. We have used 300 nodes and the time step is 10^{-9} s. This combination of space and time steps fulfils the Courant-Friedrisch-Lewy condition required for the sustainability of the numerical scheme.

Fig. 2 shows the output force (measured at the clamped end) versus the loading time for 5 m/s and several defect amplitudes: 0%, 4%, 8% and 12%. Note that the amplitude of the defects influences the force registered in the calculations, i.e. the inclusion of defects slightly modifies the average behaviour of the material. This has been observed for any combination of specimen length, applied velocity and defects amplitude. For the specific simulations shown in Fig. 2 we observe that the force is shifted upwards as the percentage increases. This is a significant point that will be further discussed in this section of the manuscript.

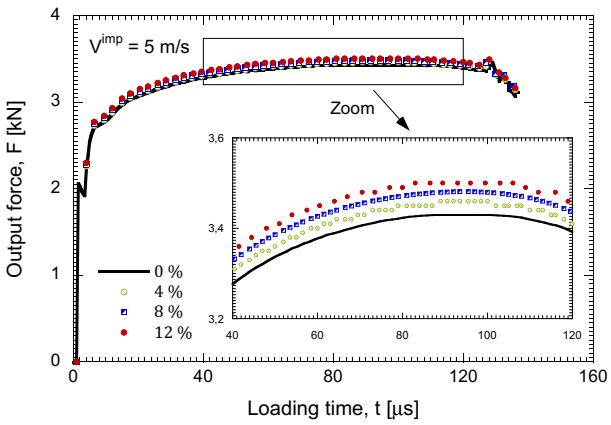

Figure 2: Output force F versus loading time t for impact velocity $V^{imp} = 5\ m/s$. Four different defect amplitudes are shown: 0%, 4%, 8% and 12%.

Fig. 3 shows the axial plastic strain rate $\dot{\varepsilon}^p_Z$ versus the normalized coordinate $\bar{Z} = Z/L$ for 5 m/s and several percentages of variation of the initial yield stress. We have selected the strain rate to carry out the analysis of our results because, due to its (intrinsic) rate-form definition, it is very sensitive to the perturbations induced by the material flaws. This allows to expose, to the full extent, the influence of the material defects in the specimen response. Two loading times are selected: $t = 30\ \mu s$ in Fig. 3(a) and $t = 116\ \mu s$ in Fig. 3(b). $t = 30\ \mu s$ corresponds to an early stage of the loading process. We observe that the strain rate

is not constant along the bar. The fluctuations are caused by the stress waves intervention within the specimen. Note that the results hardly depend on the amplitude of the defects. $t = 116\ \mu s$ corresponds to a late stage of the loading process for which the necking has already been developed. Flow localization is represented by the excursion of strain rate. The influence of defects in the location and growth rate of the necking is minimal.

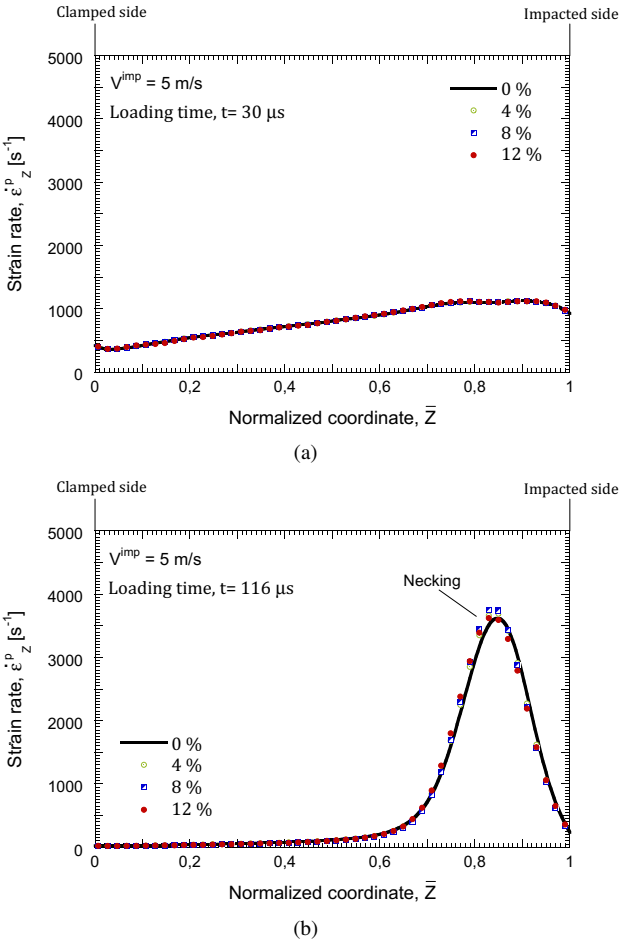

Figure 3: Axial plastic strain rate $\dot{\varepsilon}_Z^p$ versus the normalized coordinate $\bar{Z}$. Impact velocity $V^{imp} = 5\ m/s$. Four different defect amplitudes are shown: 0%, 4%, 8% and 12%. Two loading times are considered: (a) $t = 30\ \mu s$ and (b) $t = 116\ \mu s$.

Fig. 4 shows $\dot{\varepsilon}_Z^p - \bar{Z}$ curves for 10 m/s and several percentages of variation of the initial yield stress. Likewise to the case of 5 m/s, Fig. 4(a) shows that during the first stages of the loading process the influence of the inhomogeneities in the strain rate profile is negligible. Moreover, Fig. 4(b) depicts a stage of the loading process for which flow localization is already fully developed. The material defects included in the simulations barely affect the flow localization process. On the other hand, we have to point out the effect of the impact velocity in the necking location. For 5 m/s the necking developed close to the impacted side (see Fig. 3) while for 10 m/s it takes place near the clamped end (see Fig. 4). The systematic motion of the necking location along the bar with the variations in impact velocity (as experimentally observed [13, 20]) suggests that the flow localization process is deterministic and controlled, to a large extent, by the wave propagation phenomena.

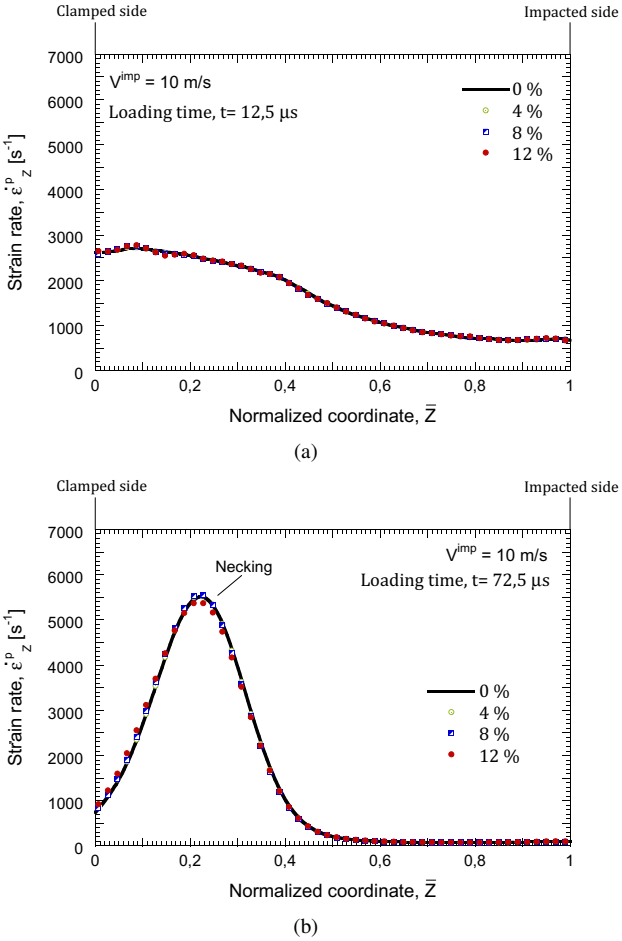

Figure 4: Axial plastic strain rate $\dot{\varepsilon}_Z^p$ versus the normalized coordinate $\bar{Z}$. Impact velocity $V^{imp} = 10\ m/s$. Four different defect amplitudes are shown: 0%, 4%, 8% and 12%. Two loading times are considered: (a) $t = 12.5\ \mu s$ and (b) $t = 72.5\ \mu s$.

Fig. 5 shows $\dot{\varepsilon}_Z^p - \bar{Z}$ curves for 15 m/s and several percentages of variation of the initial yield stress. At early stages of the loading process, Fig. 5(a), defects do not play a significant role in the strain rate profile. However, unlike what we observed for 5 m/s and 10 m/s, the inclusion of inhomogeneities in the calculations play a role in the flow localization process. In Fig. 5(b) we distinguish three scenarios:

- 0% and 2%: the results obtained for these two defect amplitudes are very similar. The necking takes places near the clamped end.
- 8% and 12%: the results obtained for these two cases have a great resemblance. The necking takes place at the centre of the specimen.

- 4% and 5%: these are transient states, halfway between the localization patterns of $0-2\%$ and $8-12\%$. As such, they reveal that the motion of necking location along the bar with the variations in the defects amplitude is not a random process. On the contrary, it is repetitive and caused by the influence of the defects in the average material behaviour (see Fig. 2).

It is apparent that, for selected loading cases, the influence of the defects in the average material behaviour is such that it affects the flow localization process.

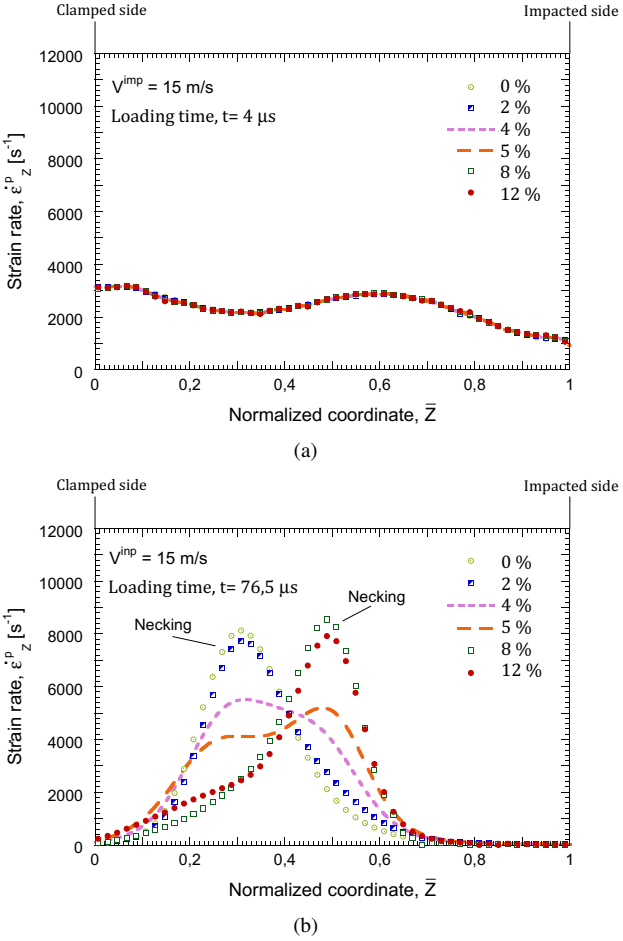

Figure 5: Axial plastic strain rate $\dot{\varepsilon}^p_Z$ versus the normalized coordinate $\bar{Z}$. Impact velocity $V^{imp} = 15\,m/s$. Six different defect amplitudes are shown: 0%, 2%, 4%, 5%, 8% and 12%. Two loading times are considered: (a) $t = 4\,\mu s$ and (b) $t = 76.5\,\mu s$.

7. Concluding remarks

In this paper we have explored, using a finite difference model, the interplay between material defects and flow localization in elastoplastic rods subjected to dynamic tension. On the one hand, we acknowledge the simplicity of our 1D numerical approach which considers idealized (localized) material flaws. On the other hand, the numerical computations developed in this paper clearly suggest that the flow localization in dynamic tensile specimens is deterministic. While material defects may play a role in the necking process, this fact does not entail that the inception of dynamic necks has random character. On the contrary, our results show that, in agreement with the experimental findings of Rittel et al. [1] and Rotbaum et al. [2], the location and development of dynamic necks is the result of the interplay between material behaviour and boundary conditions. Nevertheless, further investigations are required to check the validity of our conclusions with materials and specimens different from those used in this paper. Moreover, specific efforts need to be invested to determine the range of strain rates for which the mechanisms that control flow localization turn from imperfections-controlled [21] to inertia-controlled [7].

Acknowledgements

The authors are indebted to the Ministerio de Economía y Competitividad de España (Project DPI2014-57989-P) for the financial support received which allowed conducting this work.

Helpful discussions with Guadalupe Vadillo and Jorge Zahr are acknowledged.

References

[1] Rittel D, Rotbaum Y, Rodríguez-Martínez JA, Sory D, Zaera R. Dynamic necking of notched tensile bars: An experimental study. Experimental Mechanics 2014;54:1099–109.

[2] Rotbaum Y, Osovski S, Rittel D. Why does necking ignore notches in dynamic tension? Journal of the Mechanics and Physics of Solids 2015;78:173–85.

[3] Hu X, Daehn GS. Effect of velocity on flow localization in tension. Acta Materialia 1996;44:1021–33.

[4] Grady DE, Olsen ML. A statistics and energy based theory of dynamic fragmentation. International Journal of Impact Engineering 2003;29:293–306.

[5] Zhang H, Ravi-Chandar K. On the dynamics of necking and fragmentation - I. Real-time and post-mortem observations in Al 6061-O. International Journal of Fracture 2006;142:183–217.

[6] Zhou F, Molinari JF, Ramesh KT. An elasto-visco-plastic analysis of ductile expanding ring. International Journal of Impact Engineering 2006;33:880–91.

[7] Rodríguez-Martínez JA, Vadillo G, Fernández-Sáez J, Molinari A. Identification of the critical wavelength responsible for the fragmentation of ductile rings expanding at very high strain rates. Journal of the Mechanics and Physics of Solids 2013;61:1357–76.

[8] Rodríguez-Martínez JA, Vadillo G, Zaera R, Fernández-Sáez J. On the complete extinction of selected imperfection wavelengths in dynamically expanded ductile rings. Mechanics of Materials 2013;62:1–13.

[9] Rusinek A, Zaera R, Klepaczko JR, Cheriguene R. Analysis of inertia and scale effects on dynamic neck formation during tension of sheet steel. Acta Materialia 2005;53:5387–400.

[10] Besnard G, Hild F, Lagrange JM, Martinuzzi P, Roux S. Analysis of necking in high speed experiments by stereocorrelation. International Journal of Impact Engineering 2012;49:179–91.

[11] Holzapfel GA. Nonlinear solid mechanics: A continuum approach for engineering. Richmond, USA: John Wiley and Sons; 1 ed.; 2000.

[12] Sumelka W. The constitutive model of the anisotropy evolution for metals with microstructural defects. Ph.D. thesis; Poznan University of Technology. Faculty of Civil and Environmental Engineering; 2009.
[13] Vaz-Romero A, Rodríguez-Martínez JA, Arias A. The deterministic nature of the fracture location in the dynamic tensile testing of steel sheets. International Journal of Impact Engineering 2015;86:318–35.
[14] Rotbaum Y, Rittel D. Is there an optimal gauge length for dynamic tensile specimens? Experimental Mechanics 2015;54:1205–14.
[15] Regazzoni G, Johnson JN, Follansbee PS. Theoretical study of the dynamic tensile test. Journal of Applied Mechanics 1986;53:519–28.
[16] Ravi-Chandar K, Triantafyllidis N. Dynamic stability of a bar under high loading rate: Response to local perturbations. International Journal of Solids and Structures 2015;58:301–8.
[17] Vaz-Romero A, Rotbaum Y, Rodríguez-Martínez JA, Rittel D. Necking evolution in dynamically stretched bars: New experimental and computational insights. Journal of the Mechanics and Physics of Solids 2015;Submitted for Publication.
[18] Zaera R, Fernández-Sáez J. An implicit consistent algorithm for the integration of thermoviscoplastic constitutive equations in adiabatic conditions and finite deformations. International Journal of Solids and Structures 2006;43:1594–612.
[19] Zhang H, Ravi-Chandar K. On the dynamics of localization and fragmentation - IV. Expansion of Al 6061-O tubes. International Journal of Fracture 2010;163:41–65.
[20] Wood WW. Experimental mechanics at velocity extremes-very high strain rates. Experimental Mechanics 1965;5:361–71.
[21] Hutchinson JW, Neale KW. Influence of strain rate sensitivity on necking under uniaxial tension. Acta Metallurgica 1977;25:839–46.